Materials and Structures (2021)54:45
https://doi.org/10.1617/s11527-021-01632-x

ORIGINAL ARTICLE

Hardened properties and durability of large-scale 3D printed cement-based materials

Yu Zhang · Yunsheng Zhang · Lin Yang · Guojian Liu · Yidong Chen · Shiwei Yu · Hongjian Du

Received: 18 September 2020 / Accepted: 16 January 2021

Abstract This study systematically investigates the hardened properties, durability and void distribution of large-scale 3D printed cement-based materials (3DPC). Experimental results indicate that 3DPC has higher compressive and flexural strengths, lower drying shrinkage, better resistance against sulfate attack and carbonation than mold-cast cement-based materials, but lower resistance to frost damage and chloride ion penetration. Computed tomography scanning reveals that voids in 3DPC are strongly oriented along the printing direction. Furthermore, the voids are much more inter-connected and even continuous among the printed filaments. This unique void distribution is the origin of anisotropy for 3DPC and can explain the determined directional dependency of mechanical strengths and durability performance. Along the printing direction, the more connected voids render more channels for gas and liquid to penetrate into 3DPC.

Y. Zhang · Y. Zhang (✉) · Y. Chen
School of Materials Science and Engineering, Southeast University, Nanjing, China
e-mail: zhangys279@163.com

Y. Zhang
e-mail: zygwj88@yeah.net

Y. Zhang · Y. Zhang · Y. Chen
Collaborative Innovation Center for Advanced Civil Engineering Materials, Nanjing 211189, China

Y. Zhang
School of Civil Engineering, Lanzhou University of Technology, Lanzhou 730050, China

L. Yang
School of Water Conservancy Engineering, Zhengzhou University, Zhengzhou 450001, China

G. Liu
School of Civil Engineering, Suzhou University of Science and Technology, Suzhou 215011, China

S. Yu
Centre for Smart Infrastructure and Digital Construction, Swinburne University of Technology, VIC 3122, Australia

H. Du (✉)
Department of Civil and Environmental Engineering, National University of Singapore, Singapore 117576, Singapore
e-mail: ceedhj@nus.edu.sg

Published online: 10 February 2021

Keywords Additive manufacturing · Digital construction · Void distribution · Layer structure · Anisotropy

1 Introduction

Three-dimensional printing is a set of digital model design, information engineering, intelligent manufacturing, material engineering and many other leading technologies [1–3]. It is a rapid manufacturing technology to accumulate object through the layer-by-layer stacking. At present, this technique [4–7] has been widely applied in the fields of national defense, aerospace, automobile, medical, industrial design and jewelry.

In construction industry, 3D printing technique is used to produce buildings by adding concrete filaments layer by layer continuously through a specified nozzle [8, 9]. It reflects an obvious distinction with the conventional construction process [10]. In recent years, 3D printing technique has been tried to produce concrete component in the practical engineering. In USA, Khoshnevis [11], pioneered research by using commercial concrete as the print ink to produce a large-scale concrete-base house. In Italy [12], a 6×9 m building was fabricated by Enrico Dini and his partners through the 3DP technique (D-shape). In Spain and the Netherlands [13], 12×1.75 m and 8×3.5 m bridges were built in succession. In China [14], a 6 level building and a 2.63×3.6 m arch bridge were also printed by an extrusion-based 3D printing technique. With the development of the 3D printing concrete technique, it shows a broad application prospect in the construction field. Moreover, a large number of studies on the 3DPC has been reported [15–19], especially the hardened properties of large-scale 3DPC components.

T. T. Le et al. [20, 21] firstly reported that the high performance 3DPC has a strength of up to 102 MPa, with a strength loss of 7.3–18.2% compared to mold-cast concrete (MC), and the result of printed concrete voids mainly come from the interlayers was also concluded. Panda et al. [22, 23] found that 3DPC has an obvious directional dependency behavior at different directions, caused by the layer by layer deposition and that the printing direction governs the mechanical properties of 3DPC. Zhang et al. [24] found that the extrudability of printable concrete has a significant effect on the interlaminar bonding of 3DPC, which in turn affects the development of mechanical properties, based on the results of compressive and flexural strength as well as modulus of elasticity and Poisson's ratio.

In summary, previous studies indicate that the performance of 3DPC is strongly related to the joint among the printed filaments, even though it exhibits good mechanical strength. However, little is known about the joint in printed concrete like porosity, void size distribution, morphology, orientation, etc. At the same time, durability performance of 3DPC has been rarely reported [25]. In the future, if steel bars are used in printed concrete, the durability parameters of such concrete will be increasingly more crucial. Therefore, it is very significant to investigate the durability of 3DPC.

In this study, a systematic investigation on compressive and flexural strength, as well as resistance to frost damage, chloride ion penetration, sulfate attack and carbonation of the large–scale 3DPC components is carried out. Mercury intrusion porosimetry (MIP) and X-ray computed tomography (X-CT) are used to measure the porosity and voids distribution. Meanwhile, the performance of mould-cast specimens are measured as references. It is hoped that the study on the effect of void distribution between layers on the hardened properties and durability, which can shed light on future research of the transport of liquid and gas in 3DPC components.

2 Experimental programs

2.1 Materials and mix design

Raw materials used in this study include cement type II 52.5 (P·II 52.5), metakaolin (MK), silica fume (SF), cellulose ethers thicker agent (TA), polycarboxylate based high range water reducer (HRWR), river sand (maximum size of 1 mm), tap water and polypropylene fiber (PPF: 6 mm length and 0.2 mm diameter). The chemical composition and specific surface area (SSA) of cement, nano-clay and silica fume are shown in Table 1.

Three printable mixtures were designed based on the previous studies [24, 26], as summarized in Table 2. For each mix, the binder consists of 96

Table 1 Chemical composition and physical properties of raw materials used

Material	Chemical composition (by mass %)							L.O.I	SSA (m^2/kg)
	CaO	SiO_2	Al_2O_3	Fe_2O_3	Na_2O	MgO	SO_3		
Cement	64.85	21.65	5.56	4.32	0.24	0.84	2.58	3.07	380
Metakaolin	0.52	55.85	41.04	0.73	0.36	0.25	0.06	0.92	29,769
Silica fume	0.35	95.01	0.82	1.86	–	1.24	0.32	1.58	23,092

Table 2 Mix proportions for three printable mixtures

Mix No	Binder (wt.%)			S/B	W/B	HRWR (wt.%)	TA (wt.%)	PPF (vol.%)
	Cement	MK	SF					
M1	96	2	2	1	0.32	0.024	0.0125	–
M2	96	2	2	1.2	0.35	0.024	0.0125	–
M3	96	2	2	1	0.35	0.024	0.0125	0.4

wt.% cement, 2 wt.% MK and 2 wt.% SF. TA and HRWR are 0.0125 wt.% and 0.024 wt.%, respectively (percentage weight of binders). S/B and W/B represent sand to binder ratio and water to binder ratio, respectively. 0.4 vol.% PPF was used by the percentage of volume of the fresh mixtures. For M1 and M2, dry components were premixed for 1 min, then water with HRWR was added and mixed for another 2 min. Finally, TA was added and mixed for another 1 min. For mix M3, fibers were firstly added into sand for premixing 1 min for spreading it out evenly, then binder was added for mixing another 1 min. Next, the water with HRWR was poured in, followed by the addition of TA.

2.2 Specimens

In this study, a large concrete 3D printer operated within a 3.8 × 2.7 × 2.8 m frame was used [26]. A 1.5 × 1.5 m^2 platform which can be dragged along the Y axis was designed to hold up the printed slabs. The printing system can move along the X, Y and Z axes within a 1.5 × 1.5 × 1.5 m^3 space in accordance with the command of the control system. The 8000 mm/min moving rate of the printing nozzle and the 20 rev/min screw feed rate of the spiral twist were used in all experiments. A 12–15 mm thick and 22–24 mm wide concrete filament can be continuously printed through a Φ 20 mm nozzle.

500 × 500 × 110 mm^3 slabs were produced by this 3D printer. They were covered with a waterproof film after the printing. For the printed slab, all printed filaments are parallel to each other, as illustrated in Fig. 1. After 1 day of curing, 100 × 100 × 400 mm^3 beams and 100 mm cubes were precisely cut from the slabs. Ø100 × 50 mm^3 cylindrical specimens were cored for chloride ion penetration measurement. At the same time, fresh mixtures from the same batch as the printed slabs were also poured into steel molds to fabricate the mold-cast samples.

100 mm cube specimens were used to measure compressive strength and the resistance to carbonation and sulfate attack. Flexural strength, freeze-thawing resistance and drying shrinkage were measured using 100 × 100 × 400 mm^3 beams. All specimens were cured in an ambient temperature chamber (20 ± 2°Cand 95% ± 5% relative humidity, RH) until the testing age.

2.3 Test methods

In this study, all experiments complied with Chinese standard GB/T 50,081–2002 (Standard for test method of mechanical properties on ordinary concrete) [27] and GB/T 50,082–2009 (Standard for test methods of long-term performance and durability of ordinary concrete) [28].

The mechanical property is a critical parameter for concrete material for the structural engineering for being used. Compressive strength was tested at the age of 28 days with a loading rate of 2 kN/s. The 28-day flexural strength was evaluated by a four-point bending test. The loading rate is set as 10 N/s. The compressive and flexural strengths of MC specimens were also measured as references.

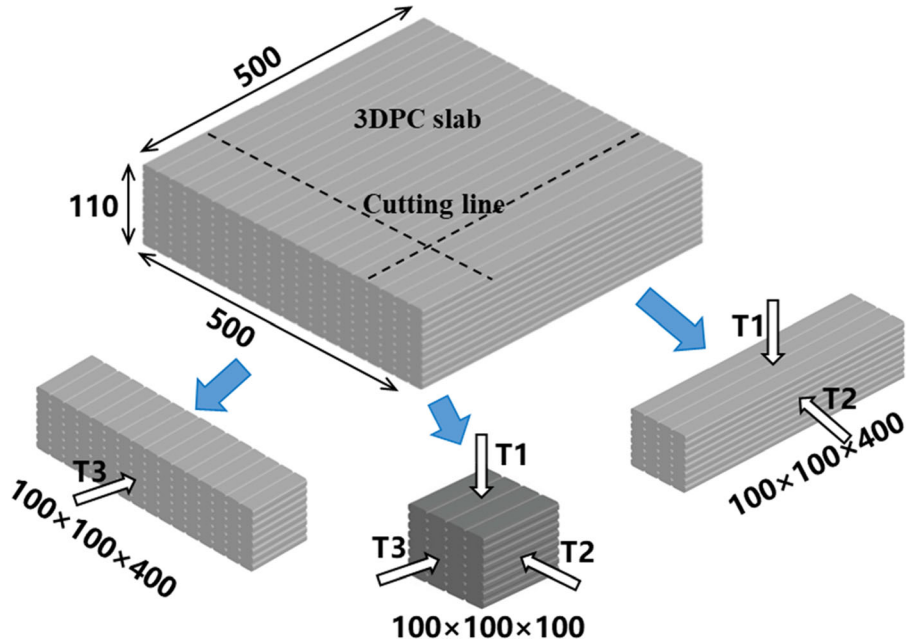

Fig. 1 Cutting diagram of 100 × 100 × 100 mm^3 cubes and 100 × 100 × 400 mm^3 beams (T is test direction)

Drying shrinkage is a critical time-dependent parameter for concrete [29, 30]. It is mainly caused by evaporation of internal water in hardened concrete [31, 32]. Large shrinkage can cause concrete to crack. Once concrete cracks, a huge contact surface area will be exposed to air and cause more water evaporation or durability issues [33, 34], which are in direct relation to the property of concrete structures. Shrinkage-induced cracking must be thus considered for large-scale 3DPC component. Two 100 × 100 × 400 mm^3 beams for each mix were used to measure the length change along T3 direction. The drying shrinkage of MC beams was also investigated as a reference. They were monitored in a shrinkage testing chamber (20 ± 2 °C and 50% RH) up to 210 days (refer to the shrinkage test in the literature [32]). Test diagram is shown in Fig. 2.

In this study, the rapid freeze-thawing experiment was carried out on 100 × 100 × 400 mm^3 beams, which were immersed into water for 28 days after cutting. Three specimens for each mix were selected for this measurement. The initial value of the transverse frequency f_0 (an ultrasonic pulse apparatus, UPV) and the initial weight W_0 of each specimen were both measured. The result of dynamic elastic modulus (tested along T3 direction) and the specimen weight loss were used to characterize the frost resistance. The dynamic elastic modulus and weight loss are calculated according to Eq. (1) and (2), respectively:

$$\mathrm{P}_n = \frac{\mathrm{f}_n^2}{\mathrm{f}_0^2} \times 100 \tag{1}$$

P_n: The relative dynamic elastic modulus of the specimen after n freeze-thawing cycles (%); f_n: The transverse frequency of the specimen after n freeze-thawing cycles; f_0: The initial value of the transverse frequency of the specimen before freeze-thawing.

$$\Delta \mathrm{W}_n = \frac{\mathrm{W}_0 - \mathrm{W}_n}{\mathrm{W}_0} \times 100 \tag{2}$$

ΔW_n: The weight loss of the specimen after n freeze-thawing cycles (%); W_n: The weight of the specimen after n freeze-thawing cycles; W_0: The initial weight of the specimen before freeze-thawing.

Chloride ion penetration test was conducted through an accelerated method in laboratory. Three Ø100 × 50 mm^3 printed specimens for each mix were measured along T1 direction, as seen in Fig. 3a. Three MC specimens were also tested as references. During the testing, the cathode was connected with a 10% NaCl solution (mass concentration), and the anode was connected with a 0.3 mol/L NaOH solution, as seen in Fig. 3b. An adjustable direct-current power

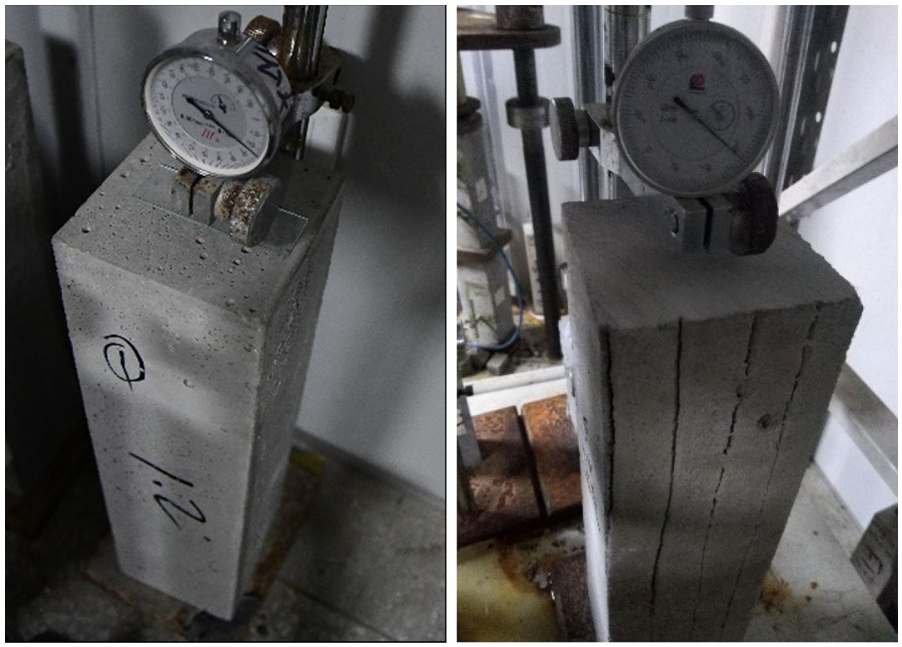

Fig. 2 Test of drying shrinkage for (left) MC and (right) 3DPC specimens

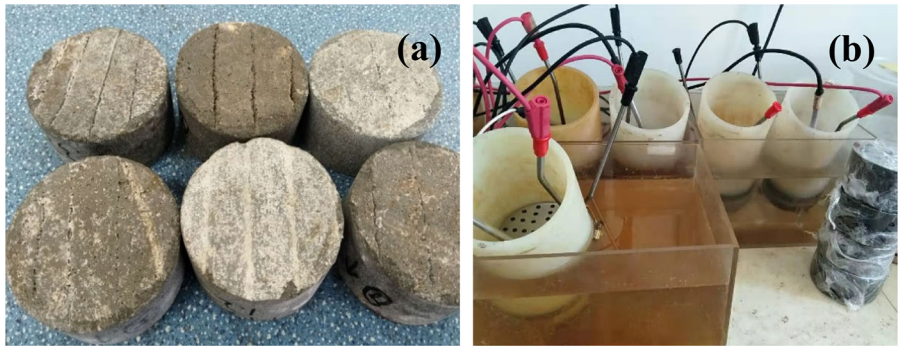

Fig. 3 **a** Coring diagram of 3DPC specimen and **b** chloride ion migration test

supply (0–60 V) was used to offer an output power. After power off, splitting the specimens in half and spraying a 0.1 mol/L $AgNO_3$ solution on the broken face. The depth of color-changed region was measured and the chloride migration coefficient was calculated by Eq. (3)

$$D_{RCM} = \frac{0.0239 \times (273 + T)L}{(U - 2)t}\left(x_d - 0.0238\sqrt{\frac{(273 + T)Lx_d}{U - 2}}\right) \quad (3)$$

D_{RCM}: Non-steady-state migration coefficient, $\times 10^{12}$ m^2/s; U: Absolute value of the applied voltage, V; T: Average value of the initial and final temperatures in the anode solution, °C; L: The height of the specimen, mm; x_d: Average value of the migration depths, mm; t: Test duration, h.

Sulfate attack to the concrete is a complex degradation process. It breaks the concrete matrix by the mechanism of the decalcification and crystallization [35, 36]. In concrete, sulfate ions can penetrate continuously into the pores and react with cement hydration products. Meanwhile, Ca^{2+} was combined with SO_4^{2-} in the concrete pores. This is an

irreversible process. The expansion process is unavoidable on account of the water absorption of reaction products in the pores [35, 37]. Hence, it is very important to characterize the erosion of sulfate ions to 3DPC. MC and 3DPC specimens were placed in an oven (80 ± 5 °C) for 48 h after curing 28 days. They were then immersed in a 5% Na_2SO_4 solution. Three 100 × 100 × 100 mm^3 specimens were tested for an average value in every 30 cycles (24 h is a cycle, alteration in wet and dry). All compressive results of 3DPC specimens were tested at T1 direction after immersion.

The resistance ability of concrete to carbonation can reflect the service life of reinforced concrete [38], to some extent. CO_2 gas can spread through the porous structure and bring in a chemical reaction with calcium hydroxide in concrete. Then the alkalinity of pore solution, which can protect steel from corrosion in concrete, will reduce [39]. Considering the application of steel reinforcement in 3DPC in future, as well as its unique feature of layered structure, it is thus very important to study carbonation resistance of 3DPC. Herein, the 100 × 100 × 100 mm^3 cubes were cut into 50 × 100 × 100 mm^3 prisms. Then they were cured at a temperature of 20 ± 2 °C and a RH of 95% for 26 days, and dried at 60 °C for 48 h. The 5 surfaces of the prisms were blocked by paraffin and then they were placed in a carbonation chamber (CO_2 concentration: 20%, RH: 70%, and T: 20 ± 2 °C) for 14, 28, 56, and 90 days. For 3DPC specimens, T2 direction was selected as the penetration direction of CO_2. After carbonation, phenolphthalein was sprayed on the freshly split section and carbonation depths were measured along the sides of section every 10 mm to calculate the average value. MC specimens were also tested as references.

The hardened properties and durability of concrete mainly depend on its porous structure. For 3DPC, some voids, like interlayer voids, were inevitable during printing. Therefore, information about void structure is critical to investigate the hardened properties and durability of 3DPC. In the present study, mix M1 was selected as the study object. Mercury intrusion porosimetry (MIP) was used to investigate the pore structure. Before MIP measurement, the concrete specimens were first broken into smaller pieces at the age of 90 days, and then the fragments less than 5 mm were cut from the center of cubes and dried in a vacuum oven for 48 h (105 °C) to constant weight. In addition, 3DPC specimens were taken from extrusion concrete filaments rather than interlayers. Simultaneously, industrial X-ray computed tomography (X-CT) was used to characterize the concrete void. As a non-destructive detecting technique [38], X-ray CT can visualize internal structures of larger specimen. It can reproduce an 2D and 3D image of a tomographic region of a scanned object by using computer process. In this study, the model of X-ray CT scanner was Y. CT Precision S (made by YXLON, Germany) and the type of detector was Y. XRD1620. The intensity of the X-ray beam after sample penetration was measured by 1024 detectors. The voltage and current of X-ray tube were 195 kV and 0.34 mA separately. The rotation angle of sample platform was 360°. 3DPC and MC specimens (100 × 100 × 100 mm^3 size) were both tested.

3 Results and discussion

3.1 Compressive and flexural strength

Figure 4 shows the compressive and flexural strength of 3DPC and MC specimens at 28 days. In Fig. 4a, it can be seen that 3DPC specimens have a higher compressive strength than that of MC specimens, though the interlayer of printed concrete does influence the compressive strength at different direction. This may be because the printed filaments were extruded and pressed against each other, which lead to a lower porosity for 3DPC than that of MC. This is different from the result in literature [41, 42]. It should be noticed that the printed components used for testing mechanical strength in literature are usually very small. They were vertically stacked by using just single layer or two adjacent layers. To a certain degree, the layers were not pressed tightly between each other in comparison with large-scale component. Therefore, there are more and larger connecting voids between the layers, which may cause a less mechanical strength than that of MC specimens. In addition, after the strong extrusion for printable concrete, the porosity of 3DPC filaments were possibly lower than that of MC concrete.

It is observed from Fig. 4b that the all flexural strengths for M1 and M2 at different directions are higher than those of MC specimens. However, the flexural strength for M3 shows a different change, the

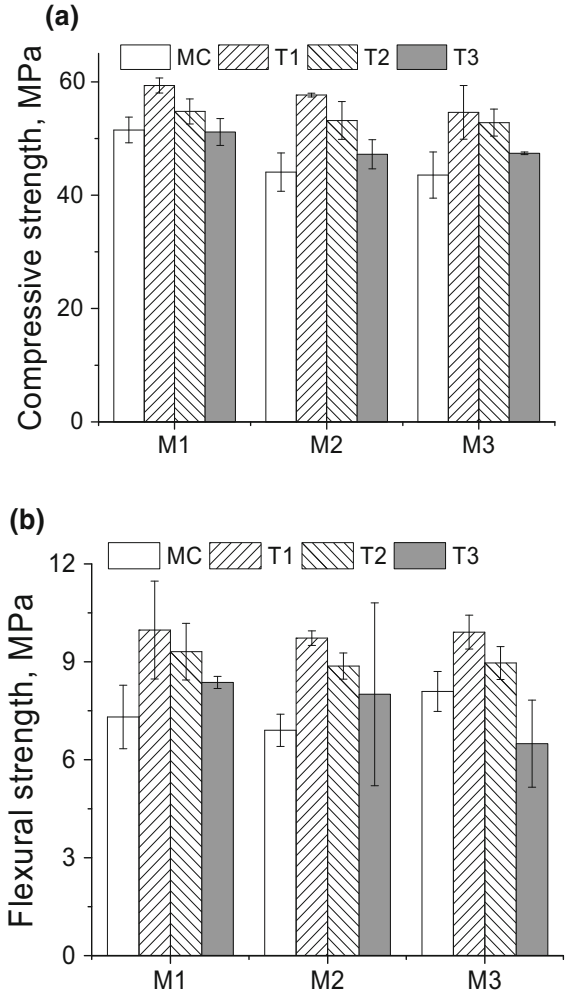

Fig. 4 **a** Compressive and **b** flexural of MC and 3DPC

strength at T3 direction is lower than that of MC specimens. This could be caused by poor extrudability of M3, which may generate many voids among the filaments and lead to a worse interlayer bond strength in printed components, especially between the adjacent layers. Additionally, the results also show that the compressive and flexural strength in the T1 direction is higher than that in both T2 and T3 directions. It can be seen from Fig. 1 that the loading directions of T1 and T2 are perpendicular to the printed concrete filaments, and T3 is parallel to it, which makes the interlayer region also parallel to the loading direction. Therefore, the strength in T3 direction is the lowest. For T1 strength higher than T2 strength, it is because the concrete filaments are flat after being extruded, and the flat surfaces are perpendicular to T1 directions, the flat sides are perpendicular to T2 direction. This result is consistent with previous studies [20, 43].

3.2 Drying shrinkage

The experimental results of drying shrinkage for three groups are shown in Fig. 5. It is seen from Fig. 5a that during the first 4 days, the drying shrinkage was almost the same for both 3DPC and MC specimens. However, the 3DPC specimens showed higher

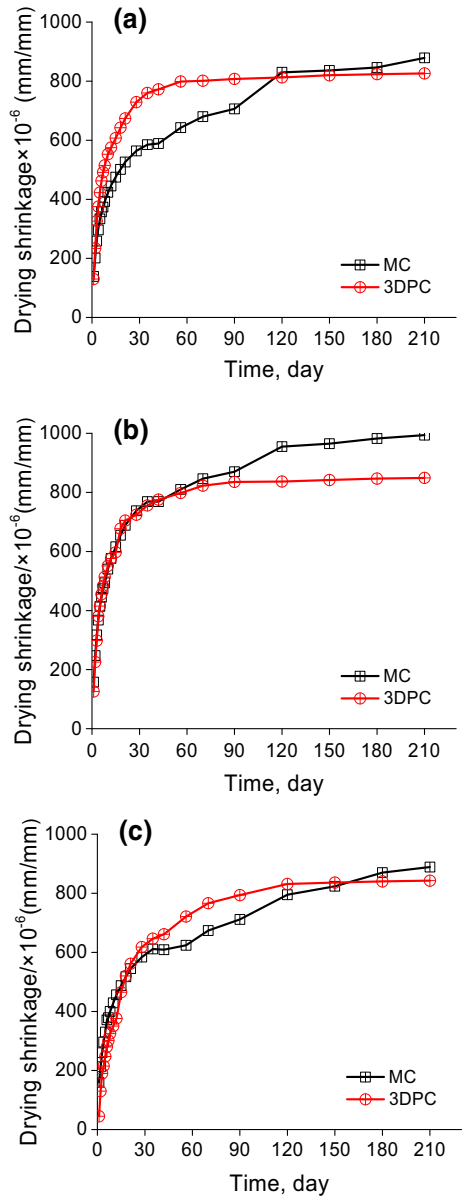

Fig. 5 Drying shrinkage of **a** M1, **b** M2 and **c** M3

shrinkage increase than MC specimens from 4 to 120 days. It is possible that the moisture evaporation rate was increased due to the interconnect voids, which was in contact with air. In a sense, the contact area between the tested specimens and the air was increased, thereby increasing the moisture evaporation rate. However, there is no such possibility for MC specimens. It can be observed that MC specimens have a slightly higher shrinkage than 3DPC specimens, when the time is exceeding 120 days. At the age of 210 days, the average value of drying shrinkage for M1 was 879×10^{-6} mm/mm (MC) and 826×10^{-6} mm/mm (3DPC), respectively.

As shown in Fig. 5b, at the first 60 days, the discrepancy between drying shrinkage of MC and 3DPC specimens of M2 mixture was small, which was unlike to the shrinkage change of M1 mixture. It may be because the interconnected void was closed due to the cutting process, thereby the contact with air was closed. While the shrinkage value of MC specimens rapidly increases after 90 days. At age of 210 days, the average amount of shrinkage for MC and 3DPC specimens was 994×10^{-6} mm/mm and 849×10^{-6} mm/mm, respectively.

Figure 5c shows a small discrepancy of drying shrinkage between MC and 3DPC specimens of M3 mixture at the first 28 days. But from 35 to 150 days, the drying shrinkage of 3DPC specimens is higher than that of MC specimens, which is similar with M1 mixture. The reason might be the same as M1 mixture. After 150 days, the drying shrinkage of MC specimen is higher than that of 3DPC specimens. At age of 210 days, their average values of drying shrinkage was 889×10^{-6} mm/mm (MC) and 843×10^{-6} mm/mm (3DPC), respectively.

In general, MC specimens have a slightly higher shrinkage than 3DPC specimens. This may be caused by the preparation process. For MC specimens, they were produced by the mold. After casting, these specimens were covered by a thin film, which can stop the water evaporation to some extent. However, the 3DPC components were produced without mold, which may cause a lot of water evaporation between concrete filaments during printing. In this way, the shrinkage of 3DPC has been accelerated in advance due to the evaporation of water. This part of the shrinkage change is not included in this testing method. Thus, more water would be lost relatively for MC specimens during the test, so the final shrinkage of MC specimens would be higher. In this research, the drying shrinkage value of printed specimens is similar to that reported by T. T. Le et al. [20].

3.3 Freeze-thawing resistance

Figure 6 illustrates the results of frost damage for MC and 3DPC series. From Fig. 6a, it is observed that the dynamic elastic modulus of concrete was reduced with the increase of freeze-thawing cycles. The critical value for dynamic elastic modulus of 60% has been not reached for all specimens until the end of the test. Therefore, for the MC and 3DPC series, the process of crack formation in the concrete has not started yet. Additionally, after 200 cycles, 3DPC specimens show a lower dynamic elastic modulus than MC specimens. However, MC specimens show higher weight loss than 3DPC specimens after freeze-thawing cycles. This is mostly because the water in the interlayer voids is continuously corroded from the interior of 3DPC spcimen under freeze-thawing environment, resulting in a lower dynamic elastic modulus than that of MC specimen. In terms of the number of freeze-thawing cycles for frost resistance assessment, M2 has a slightly better frost resistance, followed by M3 and M1. For 3DPC series, an up and down fluctuation line of dynamic modulus was noted for M1 within 200 cycles, for M2 within 300 cycles. A stable decline state was obtained for M1 after 200 cycles, for M2 after 300 cycles and for M3 after 500 cycles.

Figure 6b shows the results of weight loss with freeze-thawing cycles. In contrast to the change in dynamic elastic modulus, the weight loss of 3DPC specimen show smaller than those of MC specimen. At 1000 cycles, dynamic elastic modulus and weight loss of 95–96.2% and 3.8–7.2% for MC series as well as 82.8–92.2% and 0.3–1.9% for 3DPC series were measured. The dynamic elastic modulus is more sensitive to freeze-thawing cycles than weight loss for 3DPC specimen, which is exactly contrary to MC specimen. Figure 6c and 6d show the freeze-thawing cycles caused a very severe degradation in MC specimen, while the 3DPC spcimens were less degraded.

In view of the change in dynamic elastic modulus, 3DPC has a very poor resistance in freeze-thawing environment, in spite of its smaller weight loss. For 3DPC, a large amount of voids may exist between the layers, which may be filled with water (freezing) or ice

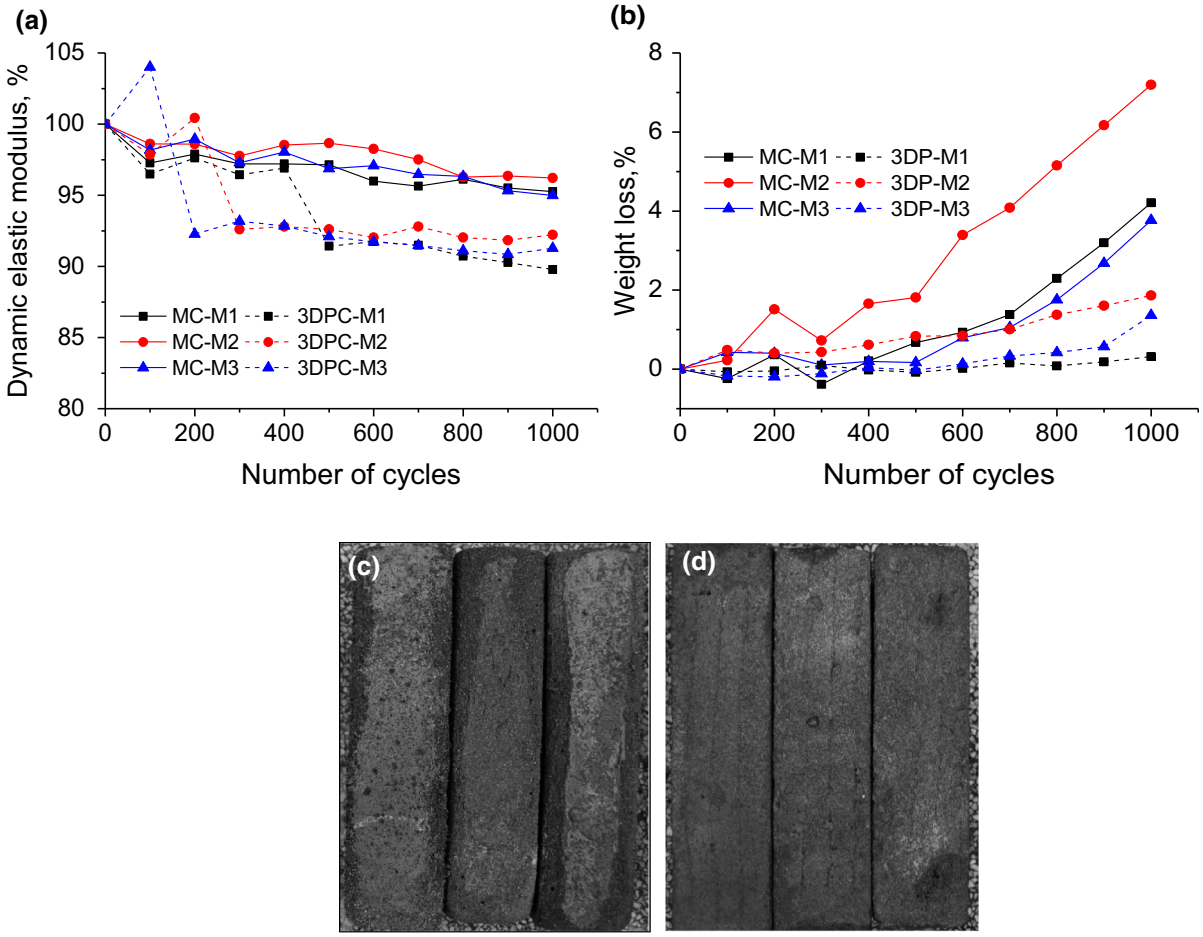

Fig. 6 **a** Relative dynamic elastic modulus and **b** weight loss during freeze-thawing cycles, and photos of **c** MC and **d** 3DPC specimen surfaces after 1000 cycles

(thawing). Thus, as the freeze-thawing, frost damage does not only occur on the surface, but may also start from the inside of concrete. However, the internally frozen debris are confined inside the specimen. On the surface of printed concrete, due to strong extrusion, it is densely packed, so the matrix is difficult to be eroded, and the aggregate is hard to be peeled off.

3.4 Chloride ion resistance

The chloride migration results for MC and 3DPC specimens are illustrated in Fig. 7. MC spcimens exhibited lower D_{RCM} than 3DPC specimens. Among 3DP series, M2 has a higher D_{RCM}, followed by M3 and M1, MC series is the same. The inset in Fig. 8 shows that there are deeper migration zones between the adjacent layers, which is similar to the result reported by Bran Anleu et al. [25]. In these regions, chloride ions transport faster and deeper throuth the interconnected or continuous voids among the filaments. In adjacent layers, interconnected voids can be easily produced, because they were less compressed than the voids between the lower and upper layers. In this regard, it is concluded that 3DPC exhibit a reduced resistance to chloride ion migration at T1 direction than MC.

3.5 Sulfate attack resistance

Figure 8 shows the results of average compressive strength for MC and 3DPC specimens which were immersed in a 5% sodium sulfate solution during a period of 5 months. It is seen that the 3DPC shows better resistance to sulfate attack than MC. For MC-

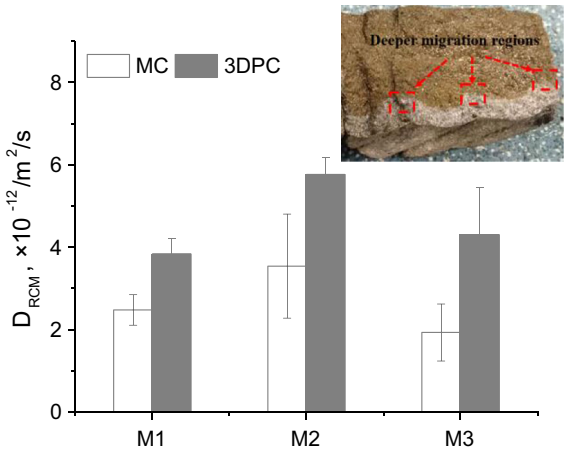

Fig. 7 Chloride migration coefficient for MC and 3DPC specimens

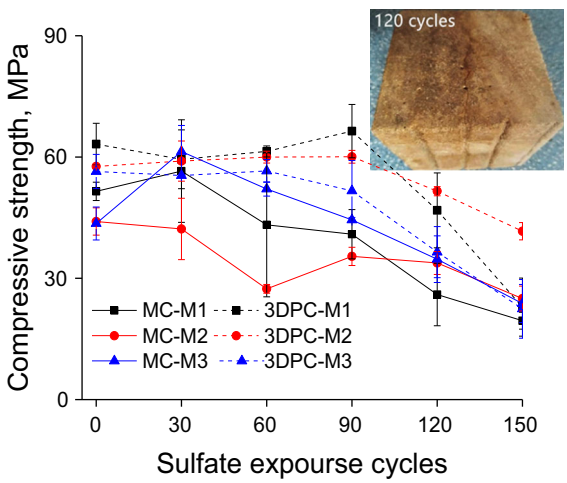

Fig. 8 Compressive strength changes with sulfate exposure period for MC and 3DPC specimens

M1 and M3, the strength reduction starts from 30 cycles, and for MC-M2, the strength reduction begins when it is corroded. As for the 3DPC-M1 and M2, the strength reduction starts from 90 cycles, and for 3DPC-M3, the strength reduction starts from 60 cycles. The increase in strength for MC concrete, during early experiment, may be generally attributed to ettringite expansion during sulfate attack [36, 37, 44]. Subsequently, the decrease in strength is due to the cavity damage caused by the water swell of ettringite. This damage does not occur until 60 cycles or even 90 cycles for 3DPC. Unlike the fact that the voids in the MC concrete are disconnected and closed, the voids among the printed concrete filaments may be connected and even continuous, the ettringite will be generated along the voids connecting direction. Therefore, the strength of 3DPC will be continuously enhanced for a period of sulfate attack.

From the inset in Fig. 8, it can be observed that the first-obvious crack of 3DPC due to sulfate attack starts to appear on the adjacent layer after 120 cycles. This indicates that the interlayer is a weak region in printed concrete when subjected to sulfate attack, especially adjacent layer. Unlike MC, the cracking of 3DPC propagates along the interlayer. As the sulfate attack progresses, the matrix failure mode is interlayer cracking rather than aggregate peeling.

3.6 Carbonation depth

Figure 9 shows the carbonation depths of MC and 3DPC specimens. It can be seen that the carbonation depth to 3DPC is less than that of MC specimen. So 3DPC has a good carbonation resistance, at least along T2 direction. Additionally, the carbonation depth increases with the increase of age. The carbonation depth of 3DPC-M1, 3DPC-M2 and 3DPC-M3 for 56-d is only 12.9 mm, 12 mm and 8.65 mm, which is less than that of MC cover thickness. Due to the CO_2 gas was required to spread from T2 direction during experiment, so the carbonation depth is as expected. The reason can be known from the inset of Fig. 9. Although the gas diffusion is through the interlayers between the lower and upper layers. As analyzed

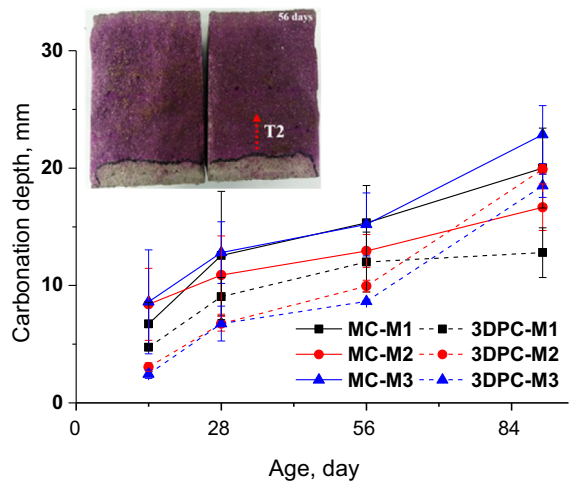

Fig. 9 Relationships between carbonation depth and age for MC and 3DPC

earlier, this region could have been pressed tightly. Therefore, it is difficult for CO_2 to pass through.

3.7 Pore structure

The identification of pore size distribution is essential to reveal the effect of pore structure on macro-performance such as mechanical strength and durability of cement-based materials. From Fig. 10a, it is observed that the intruded volume of MC obtained from MIP test is higher than that of 3DPC. It is also found that the total pore volume and total surface area of MC are slight higher than those of 3DPC. Differential intrusion curves in Fig. 10b provide extended information on pore size distribution. It can be observed that the critical pore size of 3DPC and MC is 48 nm and 57 nm, respectively. Current study points out that specimens produced by 3D printing process have lower porosity than mould-cast specimens. The 3DPC specimens were taken from extrusion filaments rather than between layers. The filaments were strongly extruded and could have a more compact structure and lower porosity.

3.8 Void distribution

The mercury intrusion test only provides part of the porous space image. Moreover, various voids between the layers for 3DPC are not easily detected by MIP test. Therefore, CT test was used to observe the interlaminar voids in this study. Figure 11 shows the 2D and 3D CT images of MC and 3DPC specimens about the voids distribution. It is noted that Top, Right and Front view were used to present the voids distribution of 2D CT image, while 3D CT images were selected to display voids with volume from 0.1 to 100 mm^3 for clarity. The CT results show that the porosity of MC concrete is 25.3%, while that of 3DPC is 5.1%. It is observed from Fig. 11a that uniform voids distribution was exhibited in MC specimen, but there are more and larger voids in comparison to 3DPC specimens. Furthermore, a large number of air voids can be found in the MC specimens. However, these voids are independent and disconnected, which is the main reason for isotropic property of MC. In Fig. 11b, voids in 3DPC specimen were mainly concentrated among the concrete filaments and they were smaller and fewer than that of MC concrete. But most of voids are connected, even continuous. This discrepancy in voids state between MC and 3DPC specimens is attributed to the different construction process.

Visibility of voids in the CT images may explain the poor flexural strength in T3 direction, the matrix is easier to break under tensile stress due to the presence of interlayer voids in comparison with compressive stress. In addition, the decrease in extrudability of the material leads to a further decrease in interlayer bonding strength [43, 44]. The significant reduction of P_n of 3DPC spcimen may be closely related to the voids among the filaments, which are connected and even continuous. When the freeze-thawing cycle is carried out, the matrix may be corroded from the inside. However, those corrosion products are enclosed in the matrix and cannot flow out, so that the internal structural of the matrix is loose. It can explain the phenomenon that the weight loss for 3DPC specimens is small while the dynamic modulus loss is large. In terms of higher migration of chloride ion and

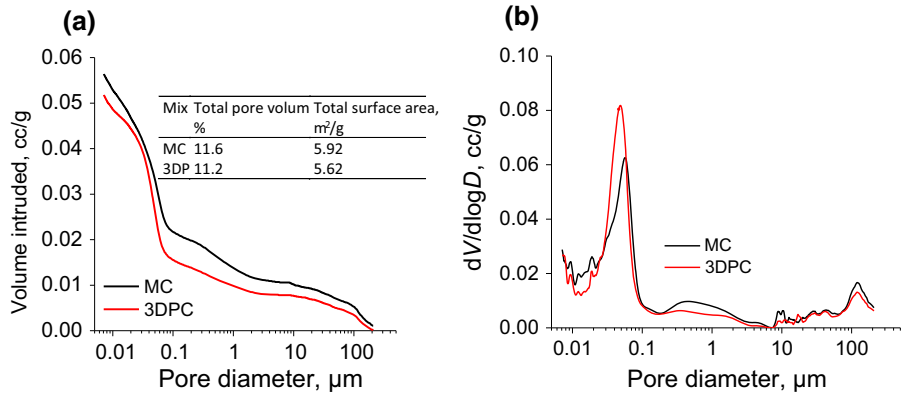

Fig. 10 **a** Volume intruded and **b** d*V*/dlog*D* of MC and 3DPC

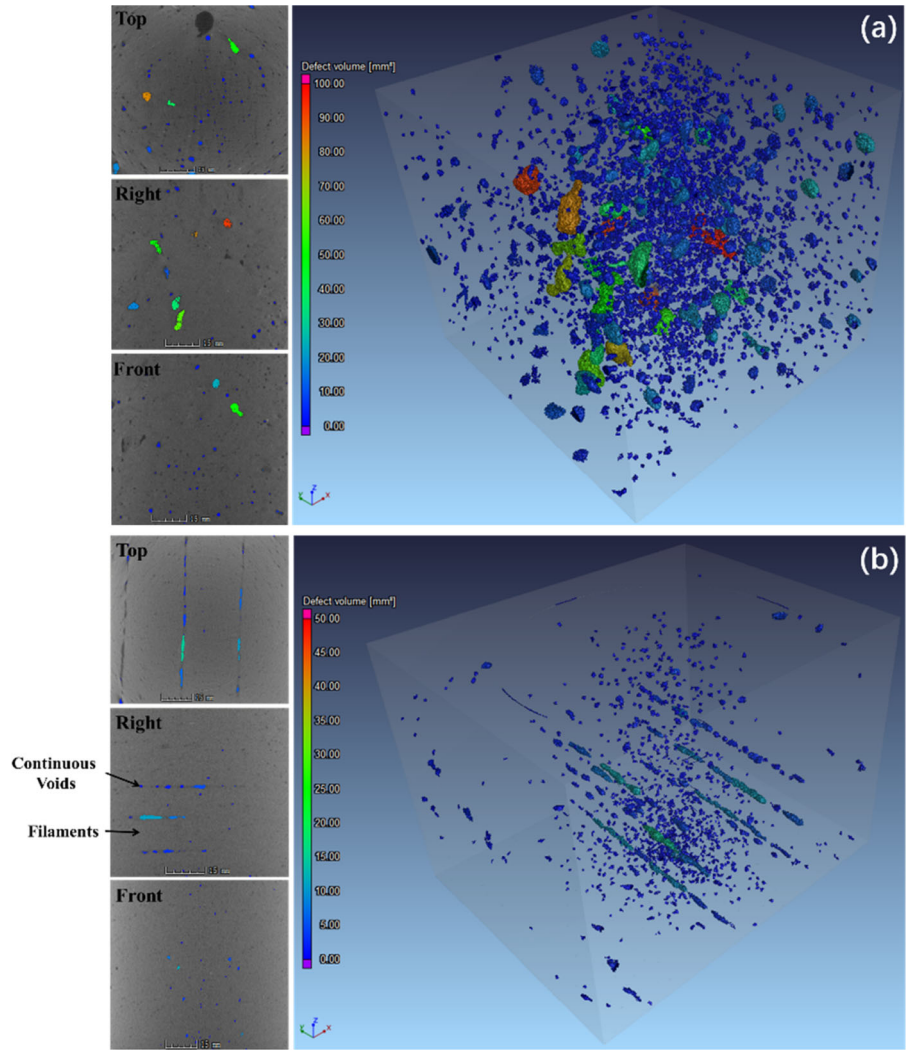

Fig. 11 CT images of **a** MC and **b** 3DPC specimens

first-obvious crack between the adjacent layers due to sulfate attack for 3DPC specimens, these results may also be attributed to the unique void system. Therefore, the connected or even continuous voids among the concrete filaments have a significant influence on the hardened properties and durability of 3DPC.

4 Conclusion

This paper has investigated the hardened properties and durability of large-scale 3DPC components. Compressive and flexural strength, resistance to frost damage, chloride ion penetration, sulfate attack and carbonation of 3DPC were systematically investigated. MIP and X-CT microscopy were employed to detect the voids distribution and to explain the macro-behavior of 3DPC. MC spcimens were also investigated as references. Based on the test data, the main conclusions are as follows:

1. CT results show that the voids in MC are larger but evenly distributed and disconnected. In contrast, the voids in 3DPC are mainly concentrated among the concrete filaments, interconnected or even continuous. This is the origin of anisotropy generally observed for 3DPC specimens.
2. 3DPC has a higher compressive and flexural strength than MC, but lower tensile strength. The

reason may be that the voids among the concrete filaments are more susceptible to damage under tensile stress compared to compressive stress.

3. 3DPC specimen has a lower long-term drying shrinkage than MC specimens, probably due to more water loss at early age.
4. 3DPC exhibits lower resistance to freeze-thawing and chloride ion migration, but better resistance to sulfate attack and carbonation (CO_2 diffusion direction is perpendicular to the printing direction) in comparison to MC specimens. Those voids are mostly interconnected or even continuous, which may lead to a corrosion from the inside of the matrix based on freeze-thawing test, a deeper migration based on rapid chloride ion migration test and a continuous enhancement at the initial stage based on sulfate attack test.

In summary, this work provides a basic study of hardened properties and durability of extrusion-based 3DPC, especially for large-scale component. The results indicate that the void connections and their preferential orientation among the printed concrete filaments obviously affect the hardened properties and durability of 3DPC. Future work on the directional property of fibers aligned by this extrusion process should be conducted.

Acknowledgements The authors gratefully acknowledge financial supports from National Natural Science Foundation of China (51878153 and 51678143), National Basic Research Program of China 973 Program (2015CB655102), National Natural Science Foundation of China (52008284) and Higher Education Institutions (20KJB560004). Support from Centre for Smart Infrastructure and Digital Construction and Faculty of Science, Engineering and Technology, Swinburne University, is appreciated.

References

1. Asprone D, Menna C, Bos FP, Salet TAM, M-Falcon J, Kaufmann W (2018) Rethinking reinforcement for digital fabrication with concrete. Cem Concr Res 112:111–121
2. Buchli J, Dörfler KD, Lussi M, Hack N, Giftthaler M, Sandy T (2018) Digital in situ fabrication-Challenges and opportunities for robotic in situ fabrication in architecture, construction, and beyond. Cem Concr Res 112:66–75
3. Damme HV (2018) Concrete material science: past, present, and future innovations. Cem Concr Res 112:5–24
4. Buswell RA, Leal WR, De Silvab WL, Jonesc SZ, Dirrenberger J (2018) 3D printing using concrete extrusion: a roadmap for research. Cem Concr Res 112:37–49
5. Buswell RA, Soar RC, Gibbb AGF, Thorpe A (2017) Freeform Construction: mega-scale rapid manufacturing for construction. Auto Constr 16:224–231
6. Mohammad S (2020) Khan, florence sanchez b, hongyu zhou, 3-D printing of concrete: beyond horizons. Cem Concr Res 133:4–14
7. Mechtcherine V, Bos FP, Perrot A, Leal da Silva WR, Nerella VN, Fataei S, Wolfs RJM, Sonebi M, Roussel N (2020) Extrusion-based additive manufacturing with cement-based materials–production steps, processes, and their underlying physics: a review. Cem Concr Res 132:106037
8. De G, Schutter K, Lesage V, Mechtcherine VN, Nerella G, Ajuanc Habert I (2018) Vision of 3D printing with concrete—technical, economic and environmental potentials. Cem Concr Res 112:25–36
9. Wangler T, Lloret E, Reiter L, Hack N, Gramazio F, Kohler M, Bernhard M, Dillenburger B, Buchli J, Roussel N, Flatt R (2016) Digital concrete: opportunities and challenges. RILEM Tech Lett 1:67–75
10. Kruger J, van Zijl G (2020) A compendious review on lack-of-fusion in digital concrete fabrication. Addit Manuf
11. Zareiyan B, Khoshnevis B (2017) Effects of interlocking on interlayer adhesion and strength of structures in 3D printing of concrete. Autom Constr 83:212–221
12. Gibbons GJ, Williams R, Purnell P, Farahi E (2013) 3D Printing of cement composites. Adv Appl Ceram 109:287–290
13. Salet TAM, Ahmed ZY, Bos FP, Laagland HLM (2018) Design of a 3D printed concrete bridge by testing. Virtual Phys Prototyp 13:222–236
14. Ju Y, Wang L, Xie HP, Ma GW, Mao LT, Zheng ZM, Lu JB (2017) Visualization of the three-dimensional structure and stress field of aggregated concrete materials through 3D printing and frozen-stress techniques. Constr Build Mater 143:121–137
15. Borg Costanzi C, Ahmed ZY, Schipper HR, Bos FP, Knaack U, Wolfs RJM (2018) 3D printing concrete on temporary surfaces: the design and fabrication of a concrete shell structure. Autom Constr 94:395–404
16. Lu B, Qian Y, Li M, Weng Y, Leong KF, Tan MJ, Qian S (2019) Designing spray-based 3D printable cementitious materials with fly ash cenosphere and air entraining agent. Constr Build Mater 211:1073–1084
17. Lowke D, Dini E, Perrot A, Weger D, Gehlen C, Dillenburger B (2018) Particle-bed 3D printing in concrete construction – possibilities and challenges. Cem Concr Res 112:50–65
18. Salet TAM, Ahmed ZY, Bos FP, Laagland HLM (2018) Design of a 3D printed concrete bridge by testing. Virtual Phys Prototyp 0:1–15
19. S. Cho, J. Kruger, S. Zeranka, A. van Rooyen, G. van Zijl (2019) Mechanical evaluation of 3D printable nano-silica incorporated fiber-reinforced lightweight foam concrete. In: proceedings of the 10th international conference on fracture mechanics of concrete and concrete structures (FRAMCOS-X)
20. Le TT, Austin SA, Lim S, Buswell RA, Law R, Gibb AGF, Thorpe T (2012) Hardened properties of high-performance printing concrete. Cem Concr Res 42:558–566

21. Le TT, Austin SA, Lim S, Buswell RA, Gibb AGF, Thorpe T (2012) Mix design and fresh properties for high-performance printing concrete. Mater Struct 45:1221–1232
22. Panda B, Paul SC, Tan MJ (2017) Anisotropic mechanical performance of 3D printed fiber reinforced sustainable construction material. Mater Lett 209:146–149
23. Panda B, Paul SC, Mohamed NAN, Tay YWD, Tan MJ (2018) Measurement of tensile bond strength of 3D printed geopolymer mortar. Measurement 113:108–116
24. Zhang Y, Zhang YS, She W, Yang L, Liu GJ, Yang YG (2019) Rheological and harden properties of the high-thixotropy 3D printing concrete. Constr Build Mater 201:278–285
25. Anleu B, Paula C (2018) Quantitative micro XRF mapping of chlorides: possibilities, limitations, and applications, from cement to digital concrete. Zurich, Switzerland, pp 117–140
26. Zhang Y, Zhang YS, Liu GJ, Yang YG, Wu M, Pang B (2018) Fresh properties of a novel 3D printing concrete ink. Constr Build Mater 174:263–271
27. GB/T 50081–2002 (2003) Standard for test method of mechanical properties on ordinary concrete
28. GB/T 50082–2009 (2010) Standard for test method of long-term performance and durability of ordinary concrete
29. Brue FNG, Davy CA, Burlion N, Skoczylas F, Bourbon X (2017) Five year drying of high performance concretes: effect of temperature and cement-type on shrinkage. Cem Concr Res 99:70–85
30. Havlásek P, Jirásek M (2016) Multiscale modeling of drying shrinkage and creep of concrete. Cem Concr Res 85:55–74
31. Kim G, Kim J-Y, Kurtis KE, Jacobs LJ (2017) Drying shrinkage in concrete assessed by nonlinear ultrasound. Cem Concr Res 92:16–20
32. Shariq M, Prasad J, Abbas H (2016) Creep and drying shrinkage of concrete containing GGBFS. Cem Concr Compos 68:35–45
33. Nehdi ML, Suleiman AR, Soliman AM (2014) Investigation of concrete exposed to dual sulfate attack. Cem Concr Res 64:42–53
34. Malolepszy J, Grabowska E (2015) Sulphate attack resistance of cement with zeolite additive. Procedia Eng 108:170–176
35. TaiIkumi SHP, Cavalaro I (2019) Segura, the role of porosity in external sulphate attack Cem. Concr Compos 97:1–12
36. Benítez P, Rodrigues F, Talukdar S, Gavilán S, Varum H, Spacone E (2019) Analysis of correlation between real degradation data and a carbonation model for concrete structures. Cem Concr Compos 95:247–259
37. Shen XH, Jiang WQ, Hou DS, Hu Z, Yang J, Liu QF (2019) Numerical study of carbonation and its effect on chloride binding in concrete. Cem Concr Compos 104:103402
38. Yang L, Zhang YS, Liu ZY, Zhao P, Liu C (2015) In-situ tracking of water transport in cement paste using X-ray computed tomography combined with CsCl enhancing. Mater Lett 160:381–383
39. Ma GW, Zhang JF, Wang L, Li ZJ, Sun JB (2018) Mechanical characterization of 3D printed anisotropic cementitious material by the electromechanical transducer. Smart Mater Struct 27(7):075036
40. Mechtcherine V, Grafe J, Nerella VN, Spaniol E, Hertel M, Füssel U (2018) 3D-printed steel reinforcement for digital concrete construction–manufacture, mechanical properties and bond behaviour. Constr Build Mater 179:125–137
41. Gosselin C, Duballet R, Roux P, Gaudillière N, Dirrenberger J, Morel P (2016) Large-scale 3D printing of ultra-high performance concrete–a new processing route for architects and builders. Mater Des 100:102–109
42. Zhang ZY, Jin XG, Luo W (2019) Long-term behaviors of concrete under low-concentration sulfate attack subjected to natural variation of environmental climate conditions. Cem Concr Res 116:217–230
43. Tang Z, Li W, Ke G, Zhou JL, Tam VWY (2019) Sulfate attack resistance of sustainable concrete incorporating various industrial solid wastes. J Clean Prod 218:810–822
44. Wolfs RJM, Bos FP, Salet TAM (2019) Hardened properties of 3D printed concrete: The influence of process parameters on interlayer adhesion. Cem Concr Res 119:132–140